



Metal–Organic Framework-Derived Hierarchical $\text{Cu}_9\text{S}_5/\text{C}$ Nanocomposite Fibers for Enhanced Electromagnetic Wave Absorption

Simeng Wu^{1,2} · Chengjuan Wang^{1,2} · Yunxiang Tang¹ · Jiangyiming Jiang¹ · Haotian Jiang^{1,2} · Xiaodan Xu^{1,2} · Bowen Cui^{1,2} · Yanyan Jiang¹ · Yanxiang Wang^{1,2}

Received: 9 September 2023 / Accepted: 19 December 2023 / Published online: 30 January 2024
© Donghua University, Shanghai, China 2024

Abstract

Refining the electromagnetic wave absorption characteristics of traditional metal–organic framework (MOF)-derived carbon composites remains a challenge because of their discontinuous conductive path. To overcome this limitation, in this work, MOF-derived hierarchical $\text{Cu}_9\text{S}_5/\text{C}$ nanocomposite fibers are fabricated by electrospinning and subsequent carbonization-sulfurization process. Morphological analyses show that MOF-derived octahedral $\text{Cu}_9\text{S}_5/\text{C}$ particles are evenly monodispersed inside carbonaceous fibers. This configuration creates a unique hierarchical structure, ranging from Cu_9S_5 particle embedding, MOF-derived skeleton, to a three-dimensional network. The optimized composite fibers ($\text{Cu}_9\text{S}_5/\text{C}$ -40) exhibit extraordinary electromagnetic wave absorption performance at a low mass fraction (20 wt%): the minimum reflection loss value reaches -69.6 dB, and the maximum effective absorption bandwidth achieves 5.81 GHz with an extremely thin thickness of only 1.83 mm. Systematic investigations demonstrate that constructing the three-dimensional conductive network to connect MOF derivatives is crucial for activating performance enhancement. The unique nano-micro hierarchical structure synergized with elaborate-configured components endows the materials with optimal impedance matching and amplifies the loss capacity of each part. This work provides a reliable example and theoretical guidance for fabricating new-generation high-efficiency MOF-derived fibrous electromagnetic wave absorbers.

Keywords Electromagnetic wave absorption · Metal–organic frameworks · Electrospinning · Cu_9S_5 · Structure-induced effect

Introduction

The vigorous development of 5G technology has heralded the arrival of the global intelligence era, while the concomitant pollution caused by electromagnetic waves (EMWs) has aroused broad public wide attention, necessitating a strict requirement for EMW absorbing materials with the characteristics of high-efficiency, lightweight, thin-thickness, and

broad-frequency [1–5]. Metal–organic framework (MOF)-derived carbon-based composites are considered attractive candidates for achieving high-efficiency absorption intensity and thin-thickness absorption bandwidth, due to their excellent traits of diversified defects, selectable components, and abundant interfaces [4–8]. Especially in recent years, transition-metal sulfides, which have higher chemical stability than metals and more abundant loss pathways than metal oxides, have captured tremendous attention for use as the second components of MOF-derived carbon-based composites [9]. For example, Xu et al. fabricated octahedral $\text{Cu}_9\text{S}_5/\text{C}$ nanoparticles and demonstrated an optimal reflection loss value of -62.3 dB with an efficient absorption bandwidth of 4.7 GHz [10]. Nevertheless, the high filling rate of MOF-derived carbon-based composites, which is generally restricted to values greater than 40 wt%, is a nonnegligible issue that violates the purpose of lightweight [11]. The fundamental causation for this characteristic is

✉ Yanxiang Wang
wyx079@sdu.edu.cn

¹ Key Laboratory for Liquid-Solid Structural Evolution and Processing of Materials Ministry of Education, Shandong University, Jinan 250061, People's Republic of China

² Carbon Fiber Engineering Research Center, School of Materials Science and Engineering, Shandong University, Jinan 250061, People's Republic of China

the discontinuity of conductive paths caused by the separation of MOF-derived particles, leading to an increase in the absorber's percolation threshold [12]. Presently, conductivity amelioration strategies, such as the increasing carbonization temperature, optimizing the component selection, and integrating with highly conductive substances (i.e., graphene, carbon nanotube.), are employed to settle this issue [13–18]. However, the first two approaches suffer from the risk of structural collapse and the inability to sufficiently increase the conductivity, respectively. Regarding integration with graphene and carbon nanotubes, the currently applied methods (direct loading and in-situ growth), cannot reconcile the precise loading and stable dispersion of MOF particles, which restricts the breakthrough of absorption performance and the design of future effective EMW absorbing agents.

Recent advancements in three-dimensional (3D) conductive network constructed by electrospinning have provided an ingenious tactic for overcoming the aforementioned obstacles. Electrospinning technology offers several significant advantages, including the uniform dispersion of particles, precise control of components, and facile fabrication [19–21]. In particular, the derived anisotropic and malleable carbonaceous fibers can provide elongated transmission pathways for carriers via an unobstructed conductive network, thus effectively reducing the percolation threshold [22, 23]. For example, our group recently reported $\text{Cu}_9\text{S}_5/\text{C}$ nanocomposite fibers with a strong absorption intensity of -65.4 dB at a low mass fraction (20 wt%) [24]. Unfortunately, because of the simple hierarchical structure and loss pathway of traditional composite fibers, impedance matching could not be adequately optimized, hence it is still difficult to achieve a satisfactory effective absorption bandwidth and matching thickness (4.1 GHz and 2.9 mm). In this context, developing new-generation MOF-derived composite fibers with hierarchical structures has emerged as a promising alternative, since composites can not only couple the multiple loss pathways of MOF derivatives and traditional fibers but also optimize impedance matching as a result of their hierarchical structures [25–27]. However, to date, there have been few studies devoted to this research direction, and efforts to modulate the absorption performance and elucidate the underlying mechanism behind are still in the initial stages.

In this work, MOF-derived hierarchical $\text{Cu}_9\text{S}_5/\text{C}$ nanocomposite fibers were fabricated by electrospinning combined with carbonization-sulfurization treatment. The architecture of a conductive network system consisting of MOF-derived particles as nodes and carbonaceous fibers as bonds was exploited to amplify conductivity. The design of a nano-micro hierarchical structure, namely, the Cu_9S_5 particle/MOF-derived skeleton/3D network, was aimed at optimizing the impedance matching and strengthening

the attenuation capability. Based on the comprehensive controllability of the structure, composition and dielectric properties, the fabricated sample exhibited excellent EMW absorption performance at a low mass fraction of 20 wt%: the minimum reflection loss value reached -69.6 dB, and the maximum effective absorption bandwidth achieved 5.81 GHz with an extremely thin thickness of only 1.83 mm. The results of the electromagnetic parameter analysis and power loss density simulation indicated that the structure-induced physical effect was essential to the improvement in EMW absorption performance. Simulations of the electric field intensity distribution and the radar cross section verified the applicability of this approach to multiple scenarios. This study performs as a meritorious reference for not only the efficient development of MOF-derived composite fibers but also theoretical analysis about the structure–functionality absorption mechanism.

Experimental Section

Materials

All reagents were of analytical grade and used directly without purification. Copper (II) nitrate trihydrate ($\text{Cu}(\text{NO}_3)_2 \cdot 3\text{H}_2\text{O}$), 1,3,5-benzenetricarboxylic acid ($\text{C}_6\text{H}_3(\text{CO}_2\text{H})_3$), and polyvinylpyrrolidone (PVP K30, MW: approx. 40,000) were obtained from Shanghai Aladdin Biochemical Technology Co., Ltd. Polyvinylpyrrolidone (PVP K88~96, MW: approx. 1,300,000), *N,N*-dimethylformamide (DMF), and thiourea ($\text{CH}_4\text{N}_2\text{S}$) were purchased from Shanghai Macklin Biochemical Technology Co., Ltd. Methanol (CH_3OH) was provided by Sinopharm Chemical Reagent Co., Ltd.

Preparation of HKUST-1-Derived Hierarchical $\text{Cu}_9\text{S}_5/\text{C}$ Nanocomposite Fibers

The preparation of HKUST-1 (a Cu-based MOF) nanoparticles is described in the Supporting Information. In a typical process, 0.933 g of HKUST-1 powder was first dispersed in 7.05 mL of DMF by sonication. Then 1.4 g of PVP k88~96 was added to the solution with vigorous stirring. The mixture was stirred for 12 h to form a homogeneously dispersed HKUST-1/PVP solution with an HKUST-1 loading of 40 wt%. The obtained solution was electrospun with a static high voltage of 12.0 kV and a collection distance of 15 cm. The as-prepared fibers were dried at 50 °C for 12 h and peroxidized at 180 °C for 3 h, followed by carbonization at 700 °C for 2 h under a N_2 atmosphere with a heating rate of 1 °C/min. Subsequently, the obtained fibers were sulfurized at 450 °C for 30 min with a heating rate of 1 °C/min under N_2 protection. Specifically, the excess thiourea

powder and carbonized fibers were placed upstream and downstream of the tubular furnace, respectively. Finally, MOF-derived hierarchical $\text{Cu}_9\text{S}_5/\text{C}$ nanocomposite fibers (denoted $\text{Cu}_9\text{S}_5/\text{C}$ -40) were obtained. For comparison, pure HKUST-1 powder and the HKUST-1/PVP fibers with different HKUST-1 load contents (0 wt%, 20 wt%, 50 wt%) were also prepared by the same processes. Accordingly, the obtained samples were denoted $\text{Cu}_9\text{S}_5/\text{C}$ -M, PVP-C, $\text{Cu}_9\text{S}_5/\text{C}$ -20, and $\text{Cu}_9\text{S}_5/\text{C}$ -50, respectively.

Electromagnetic Measurements

The obtained composites (20 wt%) and paraffin (80 wt%) were uniformly mixed at 65 °C and then pressed into a standard ring (outer diameter: 7.00 mm, inner diameter: 3.04 mm, thickness: approximately 2 mm) in a mold under a pressure of 2.5 MPa. The electromagnetic parameters in the range from 2.0 to 18.0 GHz were measured by means of a vector network analyzer (VNA; Agilent PNA N5244A) to calculate the EMW absorption properties.

Material Characterization

The compositions and crystal structures of the samples were characterized by X-ray diffraction (XRD, $\text{Cu K}\alpha$, DMAX-2500PC, Rigaku). The surface chemical states were determined by X-ray photoelectron spectroscopy (XPS, Thermo ESCALAB 250XI), and all the peaks were calibrated by considering the carbon peak at 284.8 eV as a reference. Fourier transform infrared attenuated total reflection (FTIR-ATR, Thermo Scientific Nicolet iS20) spectra were obtained in the range of 400–4000 cm^{-1} . The morphology and elemental composition were determined by using field-emission scanning electron microscopy (FE-SEM, JSM-7610F) in conjunction with energy-dispersive spectroscopy (EDS). The microstructure was investigated by high-resolution transmission electron microscopy (HR-TEM, JEOL-2100F). The thermodecomposition process and carbon content were evaluated by thermogravimetric analysis (TGA, HCT-1). To evaluate the graphitization degree of carbon, a Raman spectrometer with a 633 nm laser (LabRAM HR800) was used.

Results and Discussion

The preparation procedure for hierarchical $\text{Cu}_9\text{S}_5/\text{C}$ nanocomposite fibers is illustrated in Fig. 1a. Octahedral HKUST-1 nanoparticles were first mixed with PVP/DMF solution and then HKUST-1/PVP nanocomposite fibers were fabricated by electrospinning. After carbonization, the obtained Cu/C nanocomposite fibers developed a hierarchical and porous carbon structure. The fibers were subsequently sulfured to convert Cu to Cu_9S_5 in situ,

resulting in the formation of $\text{Cu}_9\text{S}_5/\text{C}$ nanocomposite fibers. SEM and TEM were applied to investigate the morphological and structural evolution during the synthesis of nanocomposite fibers. All the HKUST-1/PVP fibers were smoothly elongated, and octahedral HKUST-1 nanoparticles (approximately 550 nm) were uniformly monodispersed inside the PVP fibers with a diameter of approximately 300 nm [Fig. 1b(1, 2), Fig. 1e(1, 2), and Fig. S1a–d]. The carbonized and sulfurized fibers all precisely inherited the “bead-like” profile of HKUST-1/PVP fibers, accompanied by slight thermal shrinkage caused by polymer pyrolysis [Fig. S4a, Fig. 1c(1, 2), and Fig. S1e–h]. By considering the EDS mapping and spectrum [Fig. 1d(1–4) and Fig. S2], it was concluded that Cu_9S_5 nanoparticles (approximately 100 nm), generated by derived-carbon reduction and thiourea sulfurization, were uniformly embedded in the MOF-derived skeleton. Notably, carbon-based fibers with a high aspect ratio piled up with each other, acting as a bridge to connect MOF derivatives and thus constructing a 3D conductive network, which could facilitate EMW transmission and amplify conductive loss. With increasing MOF load content, the dispersion of MOF derivatives in the carbonaceous fibers became denser, which improved the electron transfer efficiency. In particular, $\text{Cu}_9\text{S}_5/\text{C}$ -50, with its closely arranged particles, was expected to exhibit the highest conductivity. More interestingly, there were abundant cavities with diameters of approximately 150 nm in the fiber matrix of $\text{Cu}_9\text{S}_5/\text{C}$ -40 in comparison to PVP-C, which were always accompanied by Cu_9S_5 nanoparticles [Fig. 1f(1) and Fig. S3]. These cavities may have formed as a result of the escape of HKUST-1’s pyrolysis gas and the diffusion of Cu ions caused by the reduced inclination of crystal surface energy. According to Garnett theory, a large number of cavities inside fibers and the interspace between fibers play crucial roles in regulating impedance matching [28]. The number of cavities increased with the MOF load, which enhanced the impedance matching optimization effect. Figure 1f(2) shows the microstructure of an obvious interface between PVP-derived carbon and the MOF derivative, which was attributed to the disparate pyrolysis characteristics in argon (Fig. S4b–d) [29]. Diversified heterogeneous interfaces and hierarchical carbon structures contributed to abundant interfacial polarization loss [30–33]. Based on the HR-TEM results [Fig. 1g(1–3)], the lattice fringes with an interplanar spacing of 0.321 nm were associated with the (0 0 15) plane of Cu_9S_5 , while the diffraction rings in the elected-area electron diffraction (SAED) pattern corresponded to the (0 1 20) and (1 1 15) planes of hexagonal Cu_9S_5 (Fig. 1h). More importantly, polycrystalline grain boundaries, along with lattice defects such as discontinuous lattice fringes and lattice distortions, were conducive to promoting defect polarization loss [34–36].

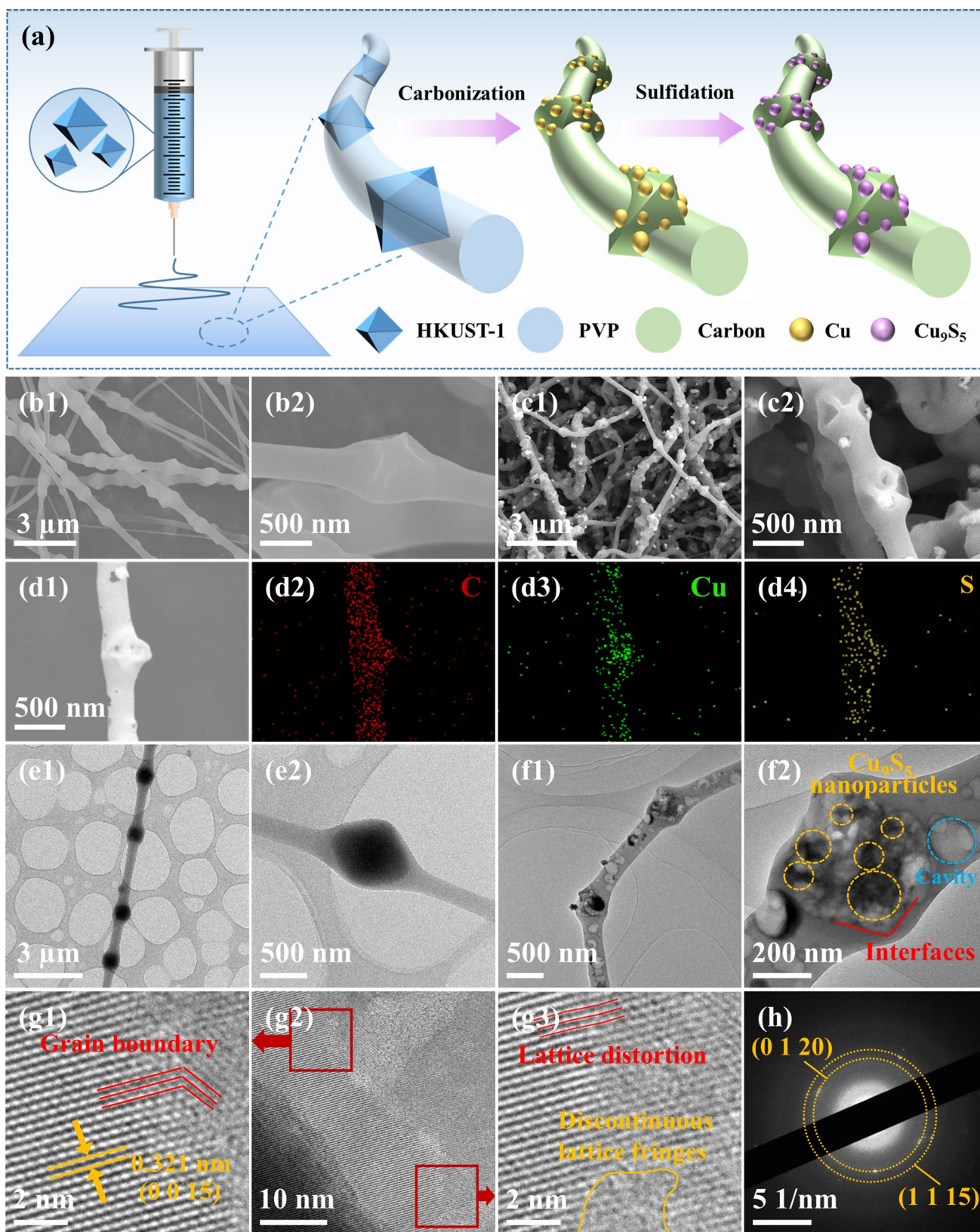


Fig. 1 Schematic of the synthetic processes for hierarchical $\text{Cu}_9\text{S}_3/\text{C}$ nanocomposite fibers (a); SEM images of 40 wt% HKUST-1/PVP nanofibers (b1, b2); SEM images of $\text{Cu}_9\text{S}_3/\text{C}$ -40 (c1, c2); elemen-

tal mappings of $\text{Cu}_9\text{S}_3/\text{C}$ -40 (d1–d4); TEM images of 40 wt% HKUST-1/PVP nanofibers (e1, e2); TEM images (f1, f2), HR-TEM images (g1–g3), and SAED pattern (h) of $\text{Cu}_9\text{S}_3/\text{C}$ -40

Taking 40 wt% HKUST-1/PVP fibers as an example, the XRD patterns and FTIR spectra confirmed the integrity of HKUST-1 (Fig. 2a and Fig. S5a), while the phase component of the carbonized fibers indicated a transformation to Cu/C (Fig. S5b). Figure 2b shows the XRD patterns of PVP-C, Cu₉S₅/C-20, Cu₉S₅/C-40, Cu₉S₅/C-50, and Cu₉S₅/C-M. The broad peak at approximately 24° was indexed to the (002) plane of graphitic microcrystals in amorphous carbon, and the other sharp and intense peaks detected at 27.7°, 29.2°, 32.1°, 41.4°, 46.1°, 54.7°, and 85.5° were assigned to the (0 0 15), (1 0 7), (1 0 10), (0 1 17), (0 0 20), (1 1 15), and (1 2 20) planes of hexagonal Cu₉S₅, respectively, confirming the successful synthesis of pure phase Cu₉S₅/C composites. In particular, the peak intensity of Cu₉S₅ increased and that of C decreased as the MOF load content increased from 0 wt% (PVP-C) to 100 wt% (Cu₉S₅/C-M), indicating the variation

in the relative content, which was relevant to the contribution degree of conductivity. The contribution of the carbon material in the composites to conductivity depended on the quality (structure and graphitization degree) and quantity (carbon content). Usually, the intensity ratio of the D-band to the G-band (I_D/I_G) in Raman spectra has a negative correlation with the graphitization degree [37, 38]. In Fig. 2c, all the samples exhibited similar graphitization degrees because they were prepared with the same carbonization temperature, deducing that the structure and carbon content actually affected the conductivity. Furthermore, TGA was applied to calculate the carbon content and the weight loss curves (Fig. 2d) were divided into three weight-change stages: the first stage involved the evaporation of adsorbed water below 150 °C; the second stage involved the pyrolysis of carbon and the oxidation of Cu₉S₅ to CuO·CuSO₄ after 300 °C;

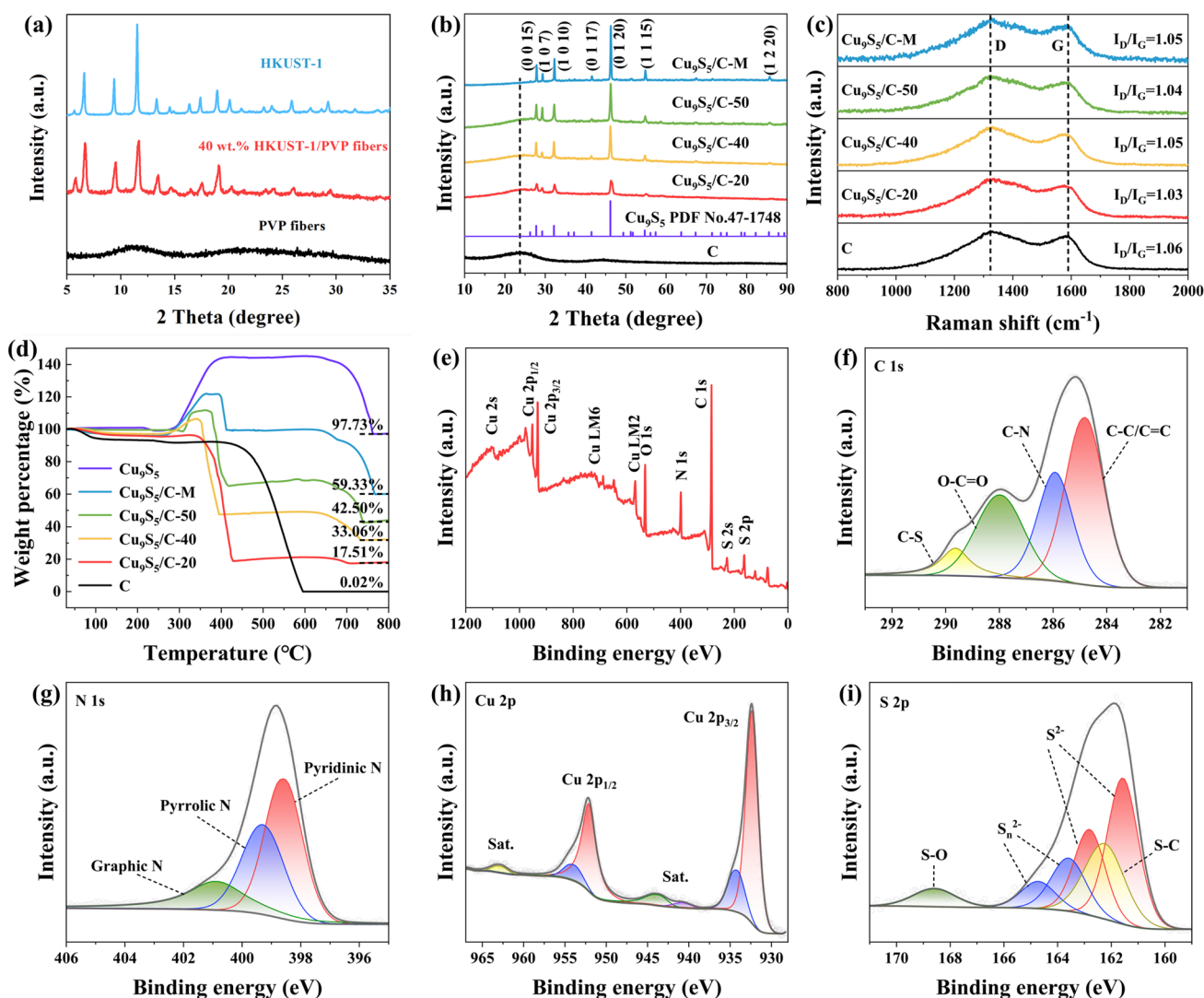


Fig. 2 XRD patterns of HKUST-1, 40 wt% HKUST-1/PVP fibers, and PVP fibers (a); XRD patterns of the as-prepared samples (b); Raman spectra of the Cu₉S₅/C nanocomposite fibers (c); TGA curves of the as-prepared samples (d); XPS high-resolution spectra of Cu₉S₅/C-40 (e–i)

the third stage involved the pyrolysis of CuSO_4 to release SO_2 and O_2 after 600 °C, ultimately forming CuO [10]. As summarized in the Supporting Information (Table S1), the carbon content decreased with increasing HKUST loading, suggesting that the effect of carbon on the conductivity of the composites was weakened. To further assess the influence of the structure and carbon content, the conductivity was measured via the four-point probe method (Fig. S5d). Although the carbon content decreased with increasing MOF loading, the conductivity increased rapidly. This phenomenon confirmed the conductivity amplification effect of the 3D conductive network structure, which played a dominant role. Experimentally, a higher conductivity can endow the composites with more conductive loss, but also lead to impedance mismatch [13]. Hence, in this work, a 3D conductive network structure in conjunction with MOF content regulation resulted in the convenient adjustment of the conductivity of the as-prepared composites and thus optimized the impedance matching.

XPS was applied to investigate the elemental composition and chemical valence states of $\text{Cu}_9\text{S}_5/\text{C}-40$. The XPS survey spectrum (Fig. 2e) verified the presence of C, N, O, Cu, and S in the composites. The high-resolution C 1 s spectrum was resolved into four peaks, as shown in Fig. 2f, which were indexed to C–C/C=C (284.8 eV), C–N (285.9 eV), O–C=O (288.0 eV), and C–S (289.6 eV) [39, 40]. Because of the suitable carbonization temperature, C–N and O–C=O were preserved during pyrolysis, while C–S was generated from doping with the H_2S produced from the decomposition of thiourea during the sulfurization process. The doped N, O, and S atoms functioned as polarization centers due to their high electronegativity and thus induced dipole polarization, which was conducive to the dissipation of electromagnetic energy [41–44]. The N 1 s spectrum (Fig. 2g) was deconvoluted into three peaks corresponding to different types of nitrogen species: graphitic-N (400.9 eV), pyrrolic-N (399.3 eV), and pyridinic-N (398.6 eV) [45]. Notably, graphitic-N could contribute unpaired electrons to conjugate with the π conjugate ring of carbon, which could assist electron transmission [46]. The Cu 2p spectrum was divided into two spin–orbit doublets, as demonstrated in Fig. 2h, the pair of peaks observed at 952.2 eV and 932.4 eV were assigned to Cu 2p_{1/2} and Cu 2p_{3/2} of Cu^+ , and the other pair centered at 954.1 eV and 934.3 eV were attributed to Cu^{2+} . Concurrently, typical satellite peaks were observed at 963.1 eV, 943.9 eV, and 940.8 eV due to the presence of Cu^{2+} [47]. Figure 2i shows the XPS spectrum of S 2p, where the spin–orbit doublets located at 164.7 eV/163.6 eV and 162.8 eV/161.6 eV were ascribed to S_n^{2-} and S^{2-} , respectively, and the two distinct peaks at 168.6 eV and 162.3 eV correspond to S–O and S–C species, respectively [47–51]. The observed S–O species presumably originated from the oxidized S source during sample synthesis. Furthermore,

S_n^{2-} was associated with sulfur vacancy, as described in a previous report, which could induce dipole polarization [34].

Based on transmission line theory and the obtained electromagnetic parameters ($\epsilon_r = \epsilon' - j\epsilon''$ and $\mu_r = \mu' - j\mu''$), the EMW absorption capability can be directly investigated in terms of the reflection loss (RL) value through Eqs. S2–3. Figure 3a–b and Fig. S6 display the 3D RL plots and the corresponding vertical images of all the samples. Generally, an RL value less than –10 dB is considered as efficient absorption, and the frequency scope corresponding to a certain thickness is defined as the effective absorption bandwidth (EAB). Apparently, $\text{Cu}_9\text{S}_5/\text{C}-\text{M}$ scarcely exhibited EMW absorption performance, whereas PVP-C exhibited a minimum reflection loss (RL_{\min}) value of –20.3 dB by virtue of natural structural advantage. After constructing the conductive networks of MOF derivatives by means of carbonaceous fibers, the EMW absorption properties of the samples were considerably enhanced: the RL_{\min} of $\text{Cu}_9\text{S}_5/\text{C}-40$ reached –69.6 dB at 7.36 GHz in 3.18 mm, and the maximum EAB achieved 5.81 GHz (12.19–18.00 GHz) with an extremely thin thickness of only 1.83 mm, which was impressive since the corresponding thickness of traditional nanocomposite fibers related to EABs is usually greater than 2 mm [24, 51]. In addition, the evaluation indices for EMW absorption performance, including RL_{\min} , EAB, and matching thickness, all displayed optimal values at the loading rate of 40 wt%. This indicates that optimizing the components allowed for effective performance adjustments. For an intuitive comparison, Fig. 3c–d shows the RL_{\min} values and EAB of all the samples with typical thicknesses. Conspicuously, $\text{Cu}_9\text{S}_5/\text{C}-40$ showed an absolute performance advantage, which confirmed the practical application value of MOF-derived conductive network engineering. In particular, one of the bottlenecks demanding breakthroughs is achieving a broader EAB with both a thin thickness and light weight, which possesses practical application significance. Therefore, a specific EAB (SEAB_{ft}) value, normalized by filler loading and matching thickness, is introduced to compare the comprehensive EAB properties of $\text{Cu}_9\text{S}_5/\text{C}-40$ with relevant previous reports. As displayed in Fig. 3e, $\text{Cu}_9\text{S}_5/\text{C}-40$ revealed an outstanding SEAB_{ft} value of 15.87 GHz mm^{–1}, far superior to almost all the reported Cu_9S_5 -based composites, binary nanocomposite fibers, and binary MOF-derived composites. Moreover, $\text{Cu}_9\text{S}_5/\text{C}-40$ was also compared with other recently reported materials, in terms of their RL_{\min} , EAB, matching thickness of EAB, filling rate, and SEAB_{ft} (Fig. 3f and Table S2) [9, 10, 13, 24, 25, 51–60]. Remarkably, $\text{Cu}_9\text{S}_5/\text{C}-40$ showed excellent integrated performance, indicating its promising application in modern microwave absorption.

The EMW absorption performance of different samples was essentially determined by electromagnetic parameters, such as the relative complex permittivity and the relative

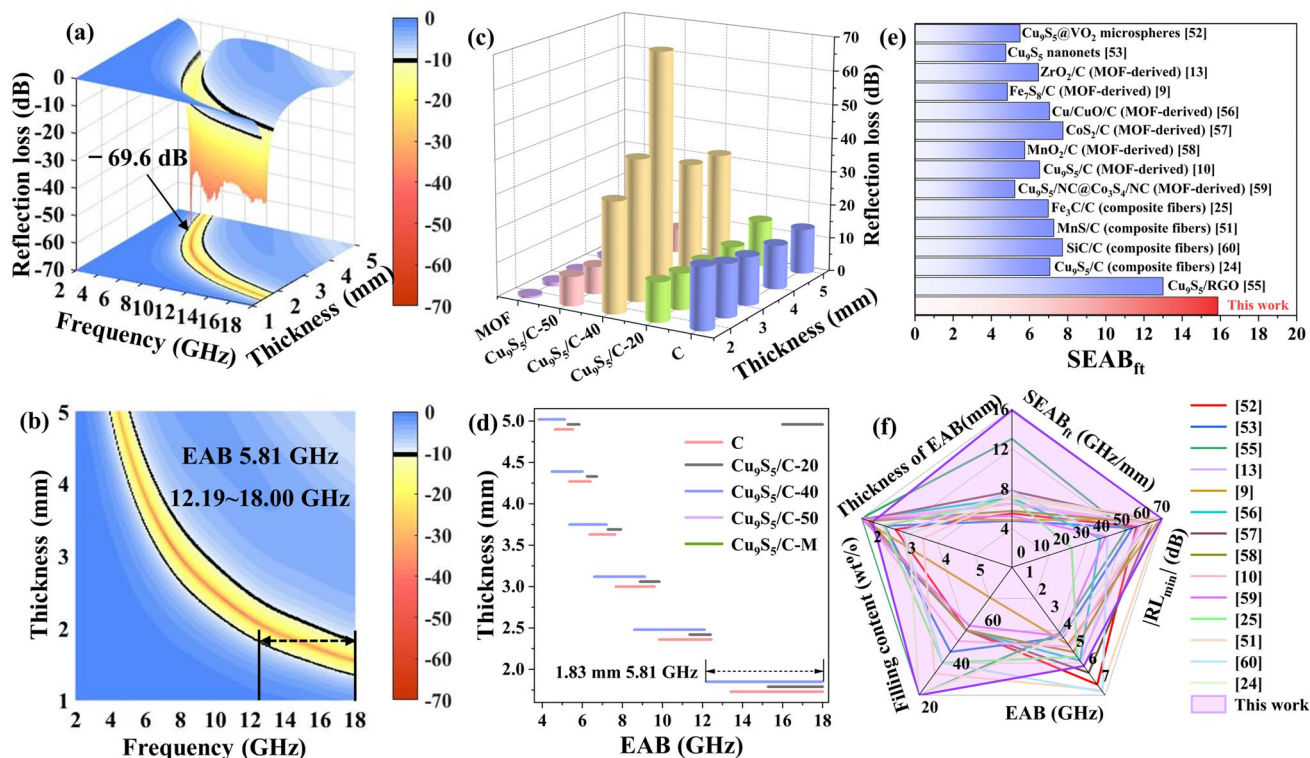


Fig. 3 3D RL diagrams and vertical view diagrams of Cu₉S₅/C-40 (a–b); RL_{min} values and EAB of as-prepared samples with typical thicknesses (c–d); SEAB_{fit} values and comprehensive indexes of Cu₉S₅/C-40 compared with relevant materials in previous reports (e–f)

complex permeability shown in Fig. 4a–b and Fig. S7a, b, d, and e. Moreover, the magnetic loss tangent and dielectric loss tangent ($\tan \mu = \mu''/\mu'$ and $\tan \varepsilon = \varepsilon''/\varepsilon'$) are important factors for calculating the magnetic loss capacity and dielectric loss capacity [61, 62]. In this work, only the relative complex permittivity was considered in view of the lack of a magnetic component (Eqs. S4–5). Theoretically, the real part and the imaginary part of the permittivity (ε' and ε'') denote the storage and dissipation capacities toward electrical energy, respectively [63, 64]. Cu₉S₅/C-M was found to possess unsatisfactory values of ε' and ε'' , which might be attributed to inefficient charge mobility caused by the noncontinuous conducting structure. Benefiting from the construction of a conductive network, the permittivity of the composites was significantly improved, far exceeding that of the pure carbonaceous fibers as the MOF loading increased to 40 wt% and 50 wt%, indicating that the favorable synergy between MOF derivatives and carbonaceous fibers could improve both the electrical energy storage and dissipation capacities of the composites. More importantly, the electromagnetic parameters were conveniently controllable by simply adjusting the MOF loading, allowing the realization of excellent EMW absorption performance. In addition, the permittivity curves showed an overall downward trend, which is the typical dispersion effect of conductive materials.

This trend was observed to be enhanced as the MOF loading increased, representing the intensified dominance of conduction loss [65]. The ε'' curves of all the samples exhibited multiple resonance peaks, implying the existence of multiple polarization relaxations. The mechanism of dielectric loss could be illustrated by Cole–Cole plots (Fig. 4c and Fig. S7h). Based on the simplified Debye equation (Eq. S6), each semicircle in the curve represents a polarization relaxation process, while the slope of the tail corresponds to the conductivity [26, 66]. Several semicircles were observed in the curves for the Cu₉S₅/C nanocomposite fibers, indicating the formation of multiple polarization processes, which were relevant to not only the dipole polarization caused by the doping atoms in the carbon matrix and the inherent defects in the Cu₉S₅ nanocrystals but also the interfacial polarization that existed at the Cu₉S₅-carbon interfaces. In addition, due to the establishment of the hierarchical structure, the composite also experienced high interface polarization caused by the hierarchical porous carbon skeleton. The establishment of a 3D conductive network, coupled with an increased proportion of MOF, resulted in an elevation of the tail slope, signifying an enhancement in conductive loss. This observation is consistent with the escalating trend of conductivity (Fig. S5d). In particular, the conductivities of Cu₉S₅/C-40 and Cu₉S₅/C-50 were much higher than those of Cu₉S₅/C-M

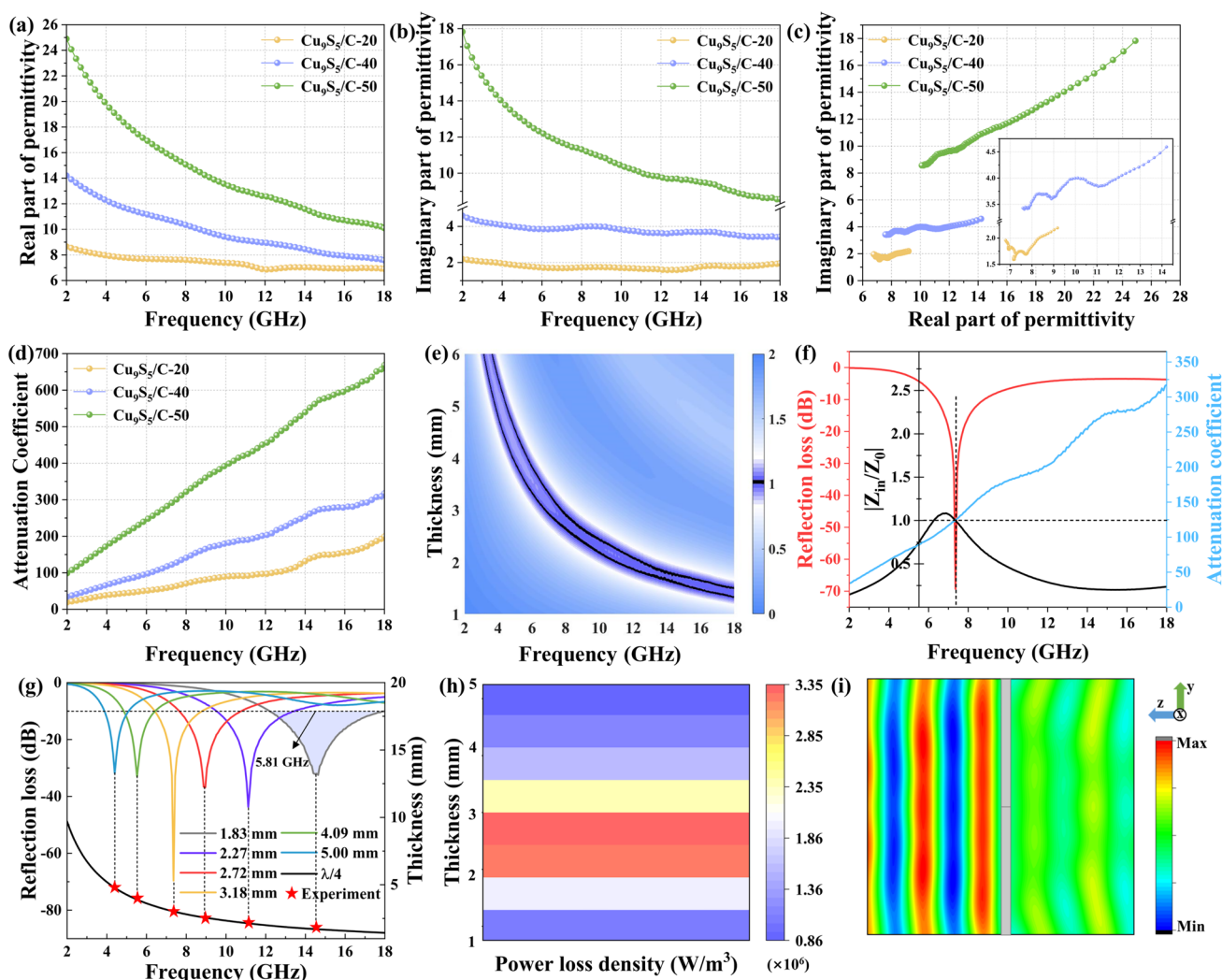


Fig. 4 The real parts (a) and imaginary parts (b) of the relative complex permittivity, Cole–Cole plots (c), and attenuation coefficient curves (d) for Cu₉S₅/C-20, Cu₉S₅/C-40, and Cu₉S₅/C-50. The imped-

ance matching diagram (e), frequency-dependent RL_{\min} , α , and Z values (f), quarter wavelength thickness matching (g), power loss density (h), and electric field intensity distribution (i) of Cu₉S₅/C-40

and pure carbonaceous fiber, which indicated that the conductive network of the MOF-derived particles and carbonaceous fiber produced a synergistic effect of $1 + 1 > 2$. Correspondingly, the total dielectric loss capacity was verified to increase in the $\tan \epsilon$ curves (Fig. S7c and g).

To explore the reasons for the excellent EMW absorption performance of Cu₉S₅/C-40, the direct factors, including the attenuation coefficient (α), impedance matching characteristic and quarter-wavelength model were analyzed by using Eqs. S7–9. α can be used to characterize the intrinsic dissipation capacity of an absorber to EMW, while the quarter-wavelength model can verify the interference cancellation behavior generated by the geometric effect of the absorber [67]. In addition, impedance matching is usually applied to assess the penetration degree of EMWs, which can be identified as perfect impedance matching and can

enable all EMWs to enter the absorber when the Z value is 1 [68, 69]. The attenuation coefficient curves are shown in Fig. 4d and Fig. S7i. The α value of Cu₉S₅/C-M was close to 0, indicating negligible dissipative capability, which led to the insufficient EMW absorption performance. Obviously, the α curves presented a progressive trend analogous to the $\tan \epsilon$ curves, but were inconsistent with the EMW absorption regularities, which was attributed to discrepancies in the impedance matching characteristics (Fig. 4e and Fig. S8). The impedance matching diagram of PVP-C displayed two slender matching regions, which proved to be unsatisfactory and resulted in inadequate EMW absorption performance. After the preparation of Cu₉S₅/C nanocomposite fibers, MOF-derived particles functioned as impedance regulators by introducing a large number of cavities into the carbonaceous fibers and cooperating with

the carbonaceous fibers to regulate conductivity. As displayed in Fig. 4e, the impedance matching characteristic of $\text{Cu}_9\text{S}_5/\text{C}-40$ was significantly optimized, resulting in a wide matching region with the widest matching frequency band at the same thickness, which was the reason for the outstanding EAB performance. In addition, due to its appropriate loading rate, $\text{Cu}_9\text{S}_5/\text{C}-40$ achieved a balance of impedance matching characteristic and attenuation capability, which endowed it with extraordinary RL performance (Fig. 4f, $Z = 1$ and $\alpha = 125$). In contrast, $\text{Cu}_9\text{S}_5/\text{C}-50$ conveyed the strongest attenuation signal, but still had ineffective absorption, which could be attributed to the impedance imbalance due to its excessive conductivity. In summary, impedance matching can be regarded as a prerequisite while the attenuation coefficient is the upper limit factor. A reasonable balance between them can obtain excellent EMW absorption performance. In addition, the experimental and

theoretical values of t_m were well matched, therefore, the interference cancellation effect was also expected to contribute to EMW dissipation (Fig. 4g). Based on Eq. S10, the power loss density was simulated to visibly illustrate the loss behavior of each sample at a typical thickness [70, 71]. As exhibited in Fig. 4h and Fig. S9, the thickness corresponding to the highest loss density showed a decreasing trend with the increase of samples' electromagnetic parameters ($\text{Cu}_9\text{S}_5/\text{C}-50 > \text{Cu}_9\text{S}_5/\text{C}-40 > \text{C} > \text{Cu}_9\text{S}_5/\text{C}-20 > \text{Cu}_9\text{S}_5/\text{C}-\text{M}$). Combined with attenuation coefficient and impedance matching analyses, this phenomenon provided us an enlightenment for reducing the matching thickness: improving the electromagnetic parameters as much as possible on the premise of ensuring impedance matching.

To verify the feasibility of practical application, CST STUDIO SUITE 2019 (a 3D electromagnetic field simulation software) was applied to simulate the electric field

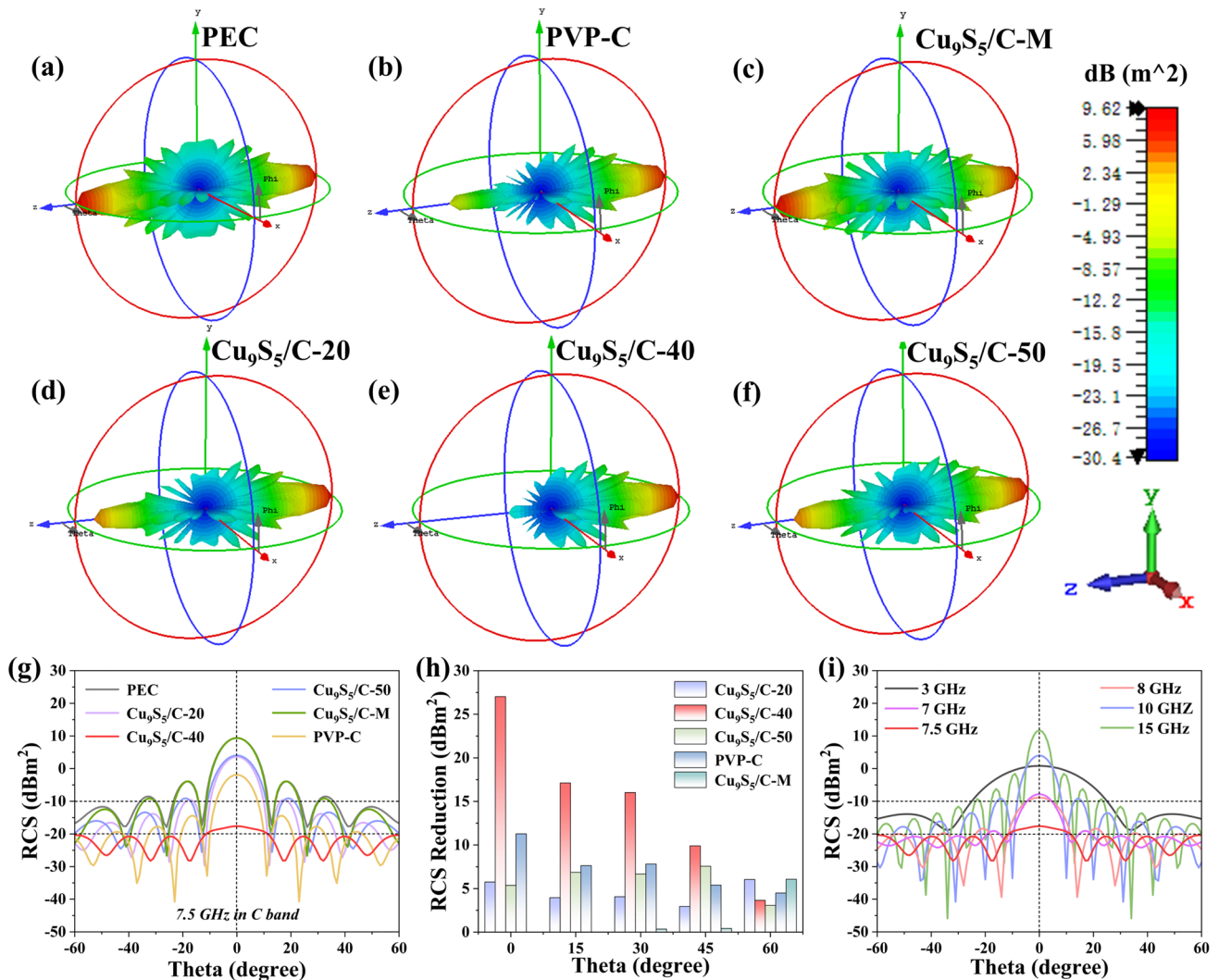


Fig. 5 The 3D RCS simulation results (a–f); the RCS curves (g) and RCS reduction values (h) of samples in the detection range of $-60^\circ \leq \theta \leq 60^\circ$; the RCS curves of $\text{Cu}_9\text{S}_5/\text{C}-40$ with 3.18 mm under typical frequency in the detection range of $-60^\circ \leq \theta \leq 60^\circ$ (i)

intensity distribution and the radar cross section (RCS) performance of the samples [70, 72]. Simulation details are provided in the Supporting Information. The electric field distribution of $\text{Cu}_9\text{S}_5/\text{C}-40$ is shown in Fig. 4i. The EMW irradiated from left to right on the absorber was located in the middle of the rectangular waveguide, leaving only a very weak electromagnetic signal on the right side, which manifested that the absorbing material itself could achieve effective absorption in the application scenario without a metal backplate. Figure 5a–f reveals the 3D far-field RCS simulation results of blank control perfect electric conductor (PEC) and the main samples. $\text{Cu}_9\text{S}_5/\text{C}-40$ showed the weakest reflected signal, demonstrating its superb electromagnetic stealth capability. Specifically, the RCS values with detection angles ranging from -60° to 60° are provided in Fig. 5g. The RCS value of $\text{Cu}_9\text{S}_5/\text{C}-40$ generally remained below -20 dBm^2 , with the RCS reduction value reaching 27 dBm^2 at 0° (Fig. 5h), surpassing those of the other samples. These characteristics significantly reduce the likelihood of the target object being detected from multiple angles. To refine the application field of $\text{Cu}_9\text{S}_5/\text{C}-40$, the simulation results of each band at 3.18 mm and 1.83 mm (the matching thickness of RL_{\min} and EAB) were taken into account

(Fig. 5i and Fig. S11). Obviously, $\text{Cu}_9\text{S}_5/\text{C}-40$ displayed the satisfactory application value in the ranges of 7.0–8.0 GHz and 13.0–18.0 GHz, which proved its potential in radar stealth and satellite communication, respectively.

Figure 6 summarizes the electromagnetic absorption mechanism of hierarchical $\text{Cu}_9\text{S}_5/\text{C}$ nanocomposite fibers. First, the specific hierarchical structures and the rational selection of MOF loading led to optimization of the electromagnetic parameters, and thus the optimal impedance matching characteristics. Second, the doping atoms in carbon and the inherent defects in Cu_9S_5 could serve as polarization centers, trapping unpaired electrons and triggering the dipole polarization effect. Third, the particular hierarchical carbon structure and abundant $\text{Cu}_9\text{S}_5/\text{C}$ interfaces contributed to the high interfacial polarization loss via the construction of a capacitance-like structure. Finally, the 3D conductive network provided a channel for the migration and hopping of carriers in carbon and Cu_9S_5 , resulting in the formation of a microcurrent amplifier to promote conductive loss. In summary, the excellent EMW absorption performance of $\text{Cu}_9\text{S}_5/\text{C}-40$ was attributed to the synergistic effect of the optimized impedance matching and the multiple loss mechanisms.

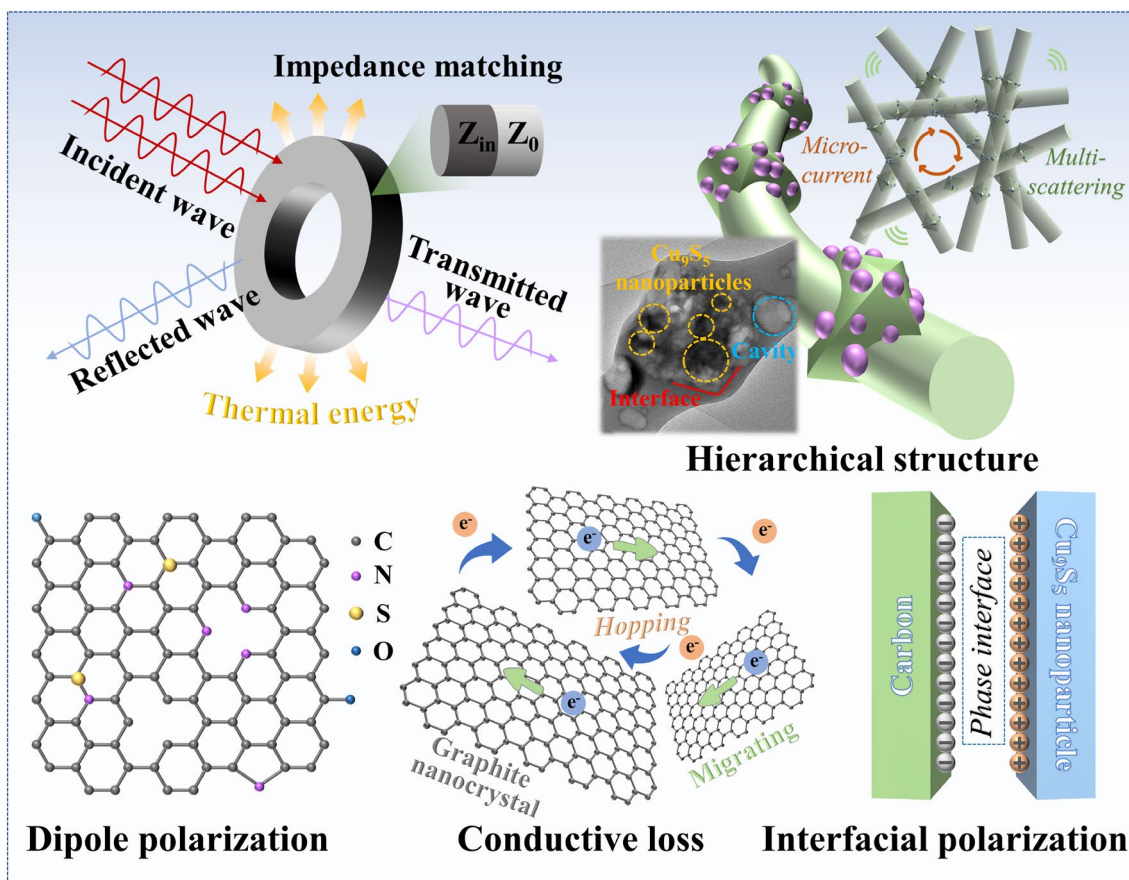


Fig. 6 Schematic diagram of the EMW absorption mechanisms of hierarchical $\text{Cu}_9\text{S}_5/\text{C}$ nanocomposite fibers

Conclusions

In this work, hierarchical Cu₉S₅/C nanocomposite fibers derived from HKUST-1/PVP fibers were prepared by electrospinning and subsequent carbonization-sulfurization process. The MOF-derived octahedral Cu₉S₅/C particles with an average sizes of approximately 550 nm were uniformly dispersed within carbonaceous fibers with an average diameter of 300 nm, creating a unique nano-micro hierarchical structure. Mechanism analysis indicated that the establishment of a 3D conductive network structure was essential in the enhancement of conductive loss. The unique hierarchical structure and the abundant lattice defects resulted in powerful interfacial polarization loss and dipole polarization loss. Based on the multiple loss coupling effect, precise regulation of the MOF loading rate enabled the coordinated balance of attenuation capacity and impedance matching. The ingenious structural design and reasonable composition regulation endowed Cu₉S₅/C-40 with excellent EMW absorption performance: the RL_{\min} of Cu₉S₅/C-40 reached -69.6 dB at 7.36 GHz with a filling rate of 20 wt%, and the maximum EAB achieved 5.81 GHz (12.19 – 18 GHz) with an extremely thin thickness of only 1.83 mm. Additionally, the electric field intensity distribution and RCS simulation showed the outstanding potential of the as-prepared composites for various applications, including radar stealth and satellite communication. This work highlights the bright prospects of MOF-derived hierarchical Cu₉S₅/C nanocomposite fibers for high-efficiency EMW absorber.

Supplementary Information The online version contains supplementary material available at <https://doi.org/10.1007/s42765-023-00362-9>.

Acknowledgements This work was supported by the Natural Science Foundation of Shandong Province (ZR2021ME194, 2022TSGC2448, 2023TSGC0545), and the key research and development program of Shandong Province(2021ZL GX01).

Data availability The data substantiating the findings of this study can be accessed from the corresponding author upon a reasonable request.

Declarations

Conflict of Interest The authors declare that they have no conflict of interest.

References

- Lv HL, Yang ZH, Pan HG, Wu RB. Electromagnetic absorption materials: current progress and new frontiers. *Prog Mater Sci.* **2022**;127: 100946.
- Wu Y, Tan SJ, Zhao Y, Liang LL, Zhou M, Ji GB. Broadband multispectral compatible absorbers for radar, infrared and visible stealth application. *Prog Mater Sci.* **2023**;135: 101088.
- Qin M, Zhang LM, Wu HJ. Dielectric loss mechanism in electromagnetic wave absorbing materials. *Adv Sci.* **2022**;9:2105553.
- Pan YL, Zhu QQ, Zhu JH, Cheng YH, Yu BY, Jia ZR, Wu GL. Macroscopic electromagnetic synergy network-enhanced N-doped Ni/C gigahertz microwave absorber with regulable microtopography. *Nano Res.* **2023**;16(7):10666–77.
- Jia ZR, Lan D, Chang M, Han Y, Wu GL. Heterogeneous interfaces and 3D foam structures synergize to build superior electromagnetic wave absorbers. *Mater Today Phys.* **2023**;37: 101215.
- Zhang X, Qiao J, Jiang YY, Wang FL, Tian XL, Wang Z, Wu LL, Liu W, Liu JR. Carbon-based MOF derivatives: emerging efficient electromagnetic wave absorption agents. *Nano-Micro Lett.* **2021**;13:135.
- Wu YL, Lan D, Ren JW, Zhang SJ. A mini review of MOFs derived multifunctional absorbents: from perspective of components regulation. *Mater Today Phys.* **2023**;36: 101178.
- Li JJ, Zhu QQ, Zhu JH, Cheng YH, Jia ZR, Lu F, Wang C, Wu GL. Inimitable 3D pyrolytic branched hollow architecture with multi-scale conductive network for microwave absorption. *J Mater Sci Technol.* **2024**;173:170–80.
- Yang YF, Xu DM, Lyu LF, Wang FL, Wang Z, Wu LL, Liu W, Liu JR. Synthesis of MOF-derived Fe₇S₈/C rod-like composites by controlled proportion of carbon for highly efficient electromagnetic wave absorption. *Compos Part A Appl Sci Manuf.* **2021**;142: 106246.
- Xu DM, Yang YF, Le K, Wang GW, Ouyang AC, Li B, Liu W, Wu LL, Wang Z, Liu JR, Wang FL. Bifunctional Cu₉S₅/C octahedral composites for electromagnetic wave absorption and supercapacitor applications. *Chem Eng J.* **2021**;417: 129350.
- Ren SN, Yu HJ, Wang L, Huang ZK, Lin TF, Huang YD, Yang J, Hong YC, Liu JY. State of the art and prospects in metal-organic framework-derived microwave absorption materials. *Nano-Micro Lett.* **2022**;14:68.
- Gao ZG, Iqbal A, Hassan T, Zhang LM, Wu HJ, Koo CM. Texture regulation of metal–organic frameworks, microwave absorption mechanism-oriented structural optimization and design perspectives. *Adv Sci.* **2022**;9:2204151.
- Zhang X, Qiao J, Liu C, Wang FL, Jiang YY, Cui P, Wang Q, Wang Z, Wu LL, Liu JR. A MOF-derived ZrO₂/C nanocomposite for efficient electromagnetic wave absorption. *Inorg Chem Front.* **2020**;7:385–93.
- Zhang X, Tian XL, Liu C, Qiao J, Liu W, Liu JR, Zeng ZH. MnCo-MOF-74 derived porous MnO/Co/C heterogeneous nanocomposites for high-efficiency electromagnetic wave absorption. *Carbon.* **2022**;149:257–66.
- Liu Y, Zeng ZH, Zheng SN, Qiao J, Liu W, Wu LL, Liu JR. Facile manufacturing of Ni/MnO nanoparticle embedded carbon nanocomposite fibers for electromagnetic wave absorption. *Compos B Eng.* **2022**;235: 109800.
- Zhang F, Jia ZR, Zhou JX, Liu JK, Wu GL, Yin PF. Metal-organic framework-derived carbon nanotubes for broadband electromagnetic wave absorption. *Chem Eng J.* **2022**;450: 138205.
- Shu RW, Li XH, Ge CQ, Wang LY. Synthesis of FeCoNi/C decorated graphene composites derived from trimetallic metal-organic framework as ultrathin and high-performance electromagnetic wave absorbers. *J Colloid Interface Sci.* **2023**;630:754–62.
- Jia ZR, Kong MY, Yu BW, Ma YZ, Pan JY, Wu GL. Tunable Co/ZnO/C@MWCNTs based on carbon nanotube-coated MOF with excellent microwave absorption properties. *J mater sci technol.* **2022**;127:153–63.
- Yang BT, Fang JF, Xu CY, Cao H, Zhang RX, Zhao B, Huang MQ, Wang XY, Lv HL, Che RC. One-dimensional magnetic FeCoNi alloy toward low-frequency electromagnetic wave absorption. *Nano-Micro Lett.* **2022**;14:170.

20. Qiao J, Zhang X, Xu DM, Kong LX, Lv LF, Yang F, Wang FL, Liu W, Liu JR. Design and synthesis of TiO₂/Co/carbon nanofibers with tunable and efficient electromagnetic absorption. *Chem Eng J.* **2020**;380: 122591.
21. Ma ML, Liao ZJ, Su XW, Zheng QX, Liu YY, Wang Y, Ma Y, Wan F. Magnetic CoNi alloy particles embedded N-doped carbonaceous fibers with polypyrrole for excellent electromagnetic wave absorption. *J Colloid Interface Sci.* **2022**;608:2203–12.
22. Wang CX, Liu Y, Jia ZR, Zhao WR, Wu GL. Multicomponent nanoparticles synergistic one-dimensional nanofibers as heterostructure absorbers for tunable and efficient microwave absorption. *Nano-Micro Lett.* **2023**;15:13.
23. Zhang S, Liu XH, Jia CY, Sun ZS, Jiang HW, Jia ZR, Wu GL. Integration of multiple heterointerfaces in a hierarchical 0D@2D@1D structure for lightweight, flexible, and hydrophobic multifunctional electromagnetic protective fabrics. *Nano-Micro Lett.* **2023**;15:204.
24. Wu SM, Qiao J, Tang YX, Zhang X, Meng XW, Hao SY, Tian HY, Li BD, Zuo XY, Liu JR, Wu LL, Wang Z, Wang FL. Heterogeneous Cu₉S₅/C nanocomposite fibers with adjustable electromagnetic parameters for efficient electromagnetic absorption. *J Colloid Interface Sci.* **2023**;630:47–56.
25. Guo RD, Su D, Chen F, Cheng YZ, Wang X, Gong RZ, Luo H. Hollow beaded Fe₃C/N-doped carbon fibers toward broadband microwave absorption. *ACS Appl Mater Interfaces.* **2022**;14:3084–94.
26. Chen JB, Zheng J, Wang F, Huang QQ, Ji GB. Carbon fibers embedded with Fe^{III}-MOF-5-derived composites for enhanced microwave absorption. *Carbon.* **2021**;174:509–17.
27. Sun RL, Yan GL, Zhang XL, Li ZY, Chen JY, Wang L, Wu YP, Wang YQ, Li H. Fe-ZIF-derived hollow porous carbon nanofibers for electromagnetic wave absorption. *Chem Eng J.* **2023**;455: 140608.
28. Yu WJ, Shao GF. Morphology engineering of defective graphene for microwave absorption. *J Colloid Interface Sci.* **2023**;640:680–7.
29. Lai QX, Zhao YX, Liang YY, He JP, Chen JH. In situ confinement pyrolysis transformation of ZIF-8 to nitrogen-enriched mesoporous carbon frameworks for oxygen reduction. *Adv Funct Mater.* **2016**;26:8334–44.
30. Rao LJ, Wang L, Yang CD, Zhang RX, Zhang JC, Liang CY, Che RC. Confined diffusion strategy for customizing magnetic coupling spaces to enhance low-frequency electromagnetic wave absorption. *Adv Funct Mater.* **2023**;33:2213258.
31. Xu HY, Li B, Jiang XY, Shi YN, Zhang X, Zhu CL, Zhang XT, Chen YJ. Fabrication of N-doped carbon nanotube/carbon fiber dendritic composites with abundant interfaces for electromagnetic wave absorption. *Carbon.* **2023**;201:234–43.
32. Wang L, Li X, Li QQ, Yu XF, Zhao YH, Zhang J, Wang M, Che RC. Oriented polarization tuning broadband absorption from flexible hierarchical ZnO arrays vertically supported on carbon cloth. *Small.* **2019**;15:1900900.
33. Liang HS, Chen G, Liu D, Li ZJ, Hui SC, Yun JJ, Zhang LM, Wu HJ. Exploring the Ni 3d orbital unpaired electrons induced polarization loss based on Ni single-atoms model absorber. *Adv Funct Mater.* **2023**;33:2212604.
34. Liu JL, Zhang LM, Zang DY, Wu HJ. A competitive reaction strategy toward binary metal sulfides for tailoring electromagnetic wave absorption. *Adv Funct Mater.* **2021**;31:2105018.
35. Chen G, Liang HS, Yun JJ, Zhang LM, Wu HJ, Wang JY. Ultrasonic field induces better crystallinity and abundant defects at grain boundaries to develop CuS electromagnetic wave absorber. *Adv Mater.* **2023**. <https://doi.org/10.1002/adma.202305586>.
36. Liang HS, Zhang LM, Wu HJ. Exploration of twin-modified grain boundary engineering in metallic copper predominated electromagnetic wave absorber. *Small.* **2022**;18:2203620.
37. Tuinstra F, Koenig JL. Raman spectrum of graphite. *J Chem Phys.* **1970**;53:1126–30.
38. Nemanich RJ, Solin SA. First- and second-order Raman scattering from finite-size crystals of graphite. *Phys Rev B.* **1979**;20:392–401.
39. Liu PB, Gao S, Wang Y, Huang Y, He WJ, Huang WH, Luo JH. Carbon nanocages with N-doped carbon inner shell and Co/N-doped carbon outer shell as electromagnetic wave absorption materials. *Chem Eng J.* **2020**;381: 122653.
40. Zhang Y, Huang YY, Srot V, Aken PAV, Maier J, Yu Y. Enhanced pseudo-capacitive contributions to high-performance sodium storage in TiO₂/C nanofibers via double effects of sulfur modification. *Nano-Micro Lett.* **2020**;12:165.
41. Shi YN, Li B, Jiang XY, Zhang X, Zhang XT, Chen YJ, Zhu CL. The enhanced dielectric property of the graphene composite anchored with non-planar iron single-atoms. *Appl Phys Lett.* **2022**;121: 073102.
42. Li B, Xu J, Xu HY, Yan F, Zhang X, Zhu CL, Zhang XT, Chen YJ. Grafting thin N-doped carbon nanotubes on hollow N-doped carbon nanoplates encapsulated with ultrasmall cobalt particles for microwave absorption. *Chem Eng J.* **2022**;435: 134846.
43. Zhang XC, Shi YN, Xu J, Ouyang QY, Zhang X, Zhu CL, Zhang XL, Chen YJ. Identification of the intrinsic dielectric properties of metal single atoms for electromagnetic wave absorption. *Nano-Micro Lett.* **2022**;14:27.
44. Xu J, Liu LN, Zhang XC, Li B, Zhu CL, Chou SL, Chen YJ. Tailoring electronic properties and polarization relaxation behavior of MoS₂ monolayers for electromagnetic energy dissipation and wireless pressure micro-sensor. *Chem Eng J.* **2021**;425: 131700.
45. Xing XL, Liu RJ, Anjass M, Cao KC, Kaiser U, Zhang GJ, Streb C. Bimetallic manganese-vanadium functionalized N, S-doped carbon nanotubes as efficient oxygen evolution and oxygen reduction electrocatalysts. *Appl Catal B.* **2020**;277: 119195.
46. Zhi DD, Li T, Qi ZH, Li JZ, Tian YR, Deng WT, Meng FB. Core-shell heterogeneous graphene-based aerogel microspheres for high-performance broadband microwave absorption via resonance loss and sequential attenuation. *Chem Eng J.* **2022**;433: 134496.
47. Yusuf M, Hira SA, Park KH. Light-harvesting novel hierarchical porous Cu₉S₅-MnWO₄ hybrid structures in photocatalytic oxidative homocoupling of alkynes and amines. *ACS Appl Mater Interfaces.* **2022**;14:15529–40.
48. Liu Y, Fang YJ, Zhao ZW, Yuan CZ, Lou XW. A ternary Fe_{1-x}S@porous carbon nanowires/reduced graphene oxide hybrid film electrode with superior volumetric and gravimetric capacities for flexible sodium ion batteries. *Adv Energy Mater.* **2019**;9:1803052.
49. Yang SS, Wang YW, Zhang HJ, Zhang Y, Liu L, Fang L, Yang XH, Gu X, Wang Y. Unique three-dimensional Mo₂C@MoS₂ heterojunction nanostructure with S vacancies as outstanding all-pH range electrocatalyst for hydrogen evolution. *J Catal.* **2019**;371:20–6.
50. Feng XT, Jiao QZ, Li Q, Shi Q, Dai Z, Zhao Y, Li HS, Feng CH, Zhou W, Feng TY. NiCo₂S₄ spheres grown on N, S co-doped rGO with high sulfur vacancies as superior oxygen bifunctional electrocatalysts. *Electrochim Acta.* **2020**;331: 135356.
51. Qiao J, Zhang X, Liu C, Zeng ZH, Yang YF, Wu LL, Wang FL, Wang Z, Liu W, Liu JR. Facile synthesis of MnS nanoparticle embedded porous carbon nanocomposite fibers for broadband electromagnetic wave absorption. *Carbon.* **2022**;191:525–34.
52. Chen WX, Xing HL, Gao ST, Yang P, Ji XL. Bi-semiconductor heterojunction Cu₉S₅@VO₂ microspheres with morphology regulation as broadband high-performance electromagnetic wave absorber. *Appl Surf Sci.* **2023**;610: 155539.

53. Tao FJ, Green M, Tran ATV, Zhang YL, Yin YS, Chen XB. Plasmonic Cu_9S_5 nanonets for microwave absorption. *ACS Appl Nano Mater.* **2019**;2:3836–47.
54. Liao J, Ye MQ, Han AJ, Guo JM, Chen CL. Nanosheet architecture of Cu_9S_5 loaded with Fe_3O_4 microspheres for efficient electromagnetic wave absorption. *Ceram Int.* **2021**;47:8803–11.
55. Liao J, Ye MQ, Han AJ, Guo JM, Liu QZ, Yu GQ. Boosted electromagnetic wave absorption performance from multiple loss mechanisms in flower-like $\text{Cu}_9\text{S}_5/\text{RGO}$ composites. *Carbon.* **2021**;177:115–27.
56. Guo YL, Chang Q, Shi ZXH, Xie JY, Yun JJ, Zhang LM, Wu HJ. Regulating conduction and polarization losses by adjusting bonded N in N-doped Cu/CuO/C composites. *J Colloid Interface Sci.* **2023**;639:444–53.
57. Yan J, Huang Y, Han XP, Gao XG, Liu PB. Metal organic framework (ZIF-67)-derived hollow CoS_2/N -doped carbon nanotube composites for extraordinary electromagnetic wave absorption. *Compos Part B Eng.* **2019**;163:67–76.
58. Yang HL, Shen ZJ, Peng HL, Xiong ZQ, Liu CB, Xie Y. 1D–3D mixed-dimensional MnO_2 @nanoporous carbon composites derived from Mn-metal organic framework with full-band ultra-strong microwave absorption response. *Chem Eng J.* **2021**;417:128087.
59. Zhu HH, Liang J, Jiao XG, Fu RR, Jiao QZ, Feng CH, Li HS, Zhang YY, Zhao Y. MOF-derived core-shell structured $\text{Cu}_9\text{S}_5/\text{NC}@\text{Co}_3\text{S}_4/\text{NC}$ composite as a high-efficiency electromagnetic wave absorber. *Ceram Int.* **2023**;49:9534–42.
60. Wang P, Cheng LF, Zhang LT. One-dimensional carbon/SiC nanocomposites with tunable dielectric and broadband electromagnetic wave absorption properties. *Carbon.* **2017**;125:207–20.
61. Cui C, Geng L, Jiang S, Bai WH, Dai LL, Jiang SX, Hu J, Ren EH, Guo RH. Construction of hierarchical carbon fiber aerogel@hollow Co_9S_8 polyhedron for high-performance electromagnetic wave absorption at low-frequency. *Chem Eng J.* **2023**;466:143122.
62. Chen XT, Wang ZD, Zhou M, Zhao Y, Tang SL, Ji GB. Multilevel structure carbon aerogels with 99.999% electromagnetic wave absorptivity at 1.8 mm and efficient thermal stealth. *Chem Eng J.* **2023**;452:139110.
63. Dou YY, Liu N, Zhang XY, Jiang WT, Jiang XH, Yu LM. Synthesis of polymer-derived N, O-doped bowl-like hollow carbon microspheres for improved electromagnetic wave absorption using controlled template pyrolysis. *Chem Eng J.* **2023**;463:142398.
64. Liu JL, Zhang LM, Wu HJ. Anion-doping-induced vacancy engineering of cobalt sulfoselenide for boosting electromagnetic wave absorption. *Adv Funct Mater.* **2022**. <https://doi.org/10.1002/adfm.202200544>.
65. Liang LY, Li QM, Yan X, Feng YZ, Wang YM, Zhang HB, Zhou XP, Liu CT, Shen CY, Xie XL. Multifunctional magnetic $\text{Ti}_3\text{C}_2\text{T}_x$ MXene/graphene aerogel with superior electromagnetic wave absorption performance. *ACS Nano.* **2021**;15:6622–32.
66. Zhang X, Tian XL, Qiao J, Fang XR, Liu KY, Liu C, Lin JP, Li LT, Liu W, Liu JR, Zeng ZH. In-situ fabrication of sustainable-N-doped-carbon-nanotube-encapsulated CoNi heterogenous nanocomposites for high-efficiency electromagnetic wave absorption. *Small.* **2023**. <https://doi.org/10.1002/sml.202302686>.
67. Cheng HR, Pan YM, Wang X, Liu CT, Shen CY, Schubert DW, Guo ZH, Liu XH. Ni flower/MXene-melamine foam derived 3D magnetic/conductive networks for ultra-efficient microwave absorption and infrared stealth. *Nano-Micro Lett.* **2022**;14:63.
68. Li MH, Zhu WJ, Li X, Xu HL, Fan XM, Wu HJ, Ye F, Xue JM, Li XQ, Cheng LF, Zhang LT. $\text{Ti}_3\text{C}_2\text{T}_x/\text{MoS}_2$ self-rolling rod-based foam boosts interfacial polarization for electromagnetic wave absorption. *Adv Sci.* **2022**;9:2201118.
69. Jiang HJ, Cai L, Pan F, Shi YY, Cheng J, Yang Y, Shi Z, Chai XL, Wu HJ, Lu W. Ordered heterostructured aerogel with broadband electromagnetic wave absorption based on mesoscopic magnetic superposition enhancement. *Adv Sci.* **2023**;10:2301599.
70. Xu J, Liu MJ, Zhang XC, Li B, Zhang X, Zhang XL, Zhu CL, Chen YJ. Atomically dispersed cobalt anchored on N-doped graphene aerogels for efficient electromagnetic wave absorption with an ultralow filler ratio. *Appl Phys Rev.* **2022**;9:011402.
71. Lan D, Wang Y, Wang YY, Zhu XF, Li HF, Guo XM, Ren JN, Guo ZH, Wu GL. Impact mechanisms of aggregation state regulation strategies on the microwave absorption properties of flexible polyaniline. *J Colloid Interface Sci.* **2023**;651:494–503.
72. Xu J, Zhang X, Zhao ZB, Hu H, Li B, Zhu CL, Zhang XT, Chen YJ. Lightweight, fire-retardant, and anti-compressed honeycombed-like carbon aerogels for thermal management and high-efficiency electromagnetic absorbing properties. *Small.* **2021**;17:2102032.



Simeng Wu is currently pursuing her Ph.D. degree under the supervision of Professor Yanxiang Wang at Shandong University. Her doctoral dissertation focuses on the application of composite carbon fiber in electromagnetic protection.



Chengjuan Wang is currently pursuing her Ph.D. degree at the School of Materials Science and Engineering, Shandong University. Her research interests focus on the preparation and multifunctional application of carbon nanotubes/carbon fiber composite materials.



Yunxiang Tang received his Bachelor's and Master's degrees from the School of Materials Science and Engineering, Liaocheng University in 2017 and 2020. Then, he continued pursuing his Ph.D. degree under the supervision of Professor Fenglong Wang at Shandong University, and his doctoral dissertation focuses on photothermal catalytic CO₂ hydrogenation.



Bowen Cui is currently pursuing his Ph.D. degree at School of Materials Science and Engineering, Shandong University. His research focuses on the mechanism of catalytic growth of carbon nanotubes on the surface of continuous carbon fibers.



Jiangyiming Jiang is currently pursuing his Ph.D. degree under the supervision of Professor Yun Tian at the School of Materials Science and Engineering, Shandong University. His research is focus on the semiconductor thin film materials and their application for thin film transistors and solar cells.



Yanyan Jiang completed her Ph.D. in Prof. Martina Stenzel group, School of Chemical Engineering at the University of New South Wales, Australia in 2016. She was awarded (2016) Japan Society for Promotion of Science (JSPS) Postdoctoral Research Fellowship at Kyoto University under the supervision of Prof. Itaru Hamachi. Since 2018, she has been appointed as a full professor of materials science and engineering at Shandong University. Her research interests are in the synthesis of functional nano-

particles serving as anti-cancer drug carriers, biosensors, nanoenzyme, and theoretical studies of the mechanism and properties of these nanoparticles.



Haotian Jiang is currently pursuing his Ph.D. degree at School of Materials Science and Engineering, Shandong University. His research focuses on the application of carbon nanofibers in electromagnetic wave absorption.



Yanxiang Wang received his Ph.D. degree in the School of Materials Science and Engineering, Shandong University in 2003. Now he is a full professor in the School of Materials Science and Engineering at Shandong University. His research interests are the preparation and characterization of carbon materials and their functional composite fibers, such as polyacrylonitrile, graphene, and carbon fibers. In the last five years, he has published more than 80 research papers in internationally

reputed journals.



Xiaodan Xu is currently pursuing her Ph.D. degree at School of Materials Science & Engineering, Shandong University. Her research focuses on the preparation of MXene-based materials, and their application in electromagnetic protection and electrochemical performance.